Polymer 54 (2013) 5936–5941

Contents lists available at ScienceDirect

Polymer

journal homepage: www.elsevier.com/locate/polymer

Carbon nanopatterns and nanoribbons from directly nanoimprinted polyacrylonitrile: Correlation between crystallite orientation and nanoimprint process

Zheng Zhang [a,*], Daniela Molina Piper [a], Seoung-Bum Son [b], Seul Cham Kim [b], Kyu Hwan Oh [b], Se-Hee Lee [a], Yifu Ding [a,*]

[a] Department of Mechanical Engineering, University of Colorado, Boulder, CO 80309-0427, United States
[b] Department of Materials Science and Engineering, Seoul National University, Seoul 151-742, Republic of Korea

ARTICLE INFO

Article history:
Received 24 June 2013
Accepted 28 July 2013
Available online 6 August 2013

Keywords:
Carbon nanostructure
Polyacrylonitrile
Nanoimprint lithography

ABSTRACT

We present the fabrication of lithographically defined carbon patterns and nanoribbons using a common carbon precursor, polyacrylonitrile (PAN). This method is based on nanoimprint lithography and has been demonstrated to be reliable and capable of nanofabrication over a large surface area at low cost, compared with current carbon-patterning techniques. Most interestingly, the deformation profile of the PAN during the imprinting process resulted in a distribution of aligned PAN chains within the patterns, which led to a similar anisotropic correlation of the carbon crystallites in the carbonized structures.

1. Introduction

Carbon-based nanostructures are promising for many emerging technologies [1–3]; this is due to their outstanding electrical and mechanical properties, chemical tolerance and high-temperature endurance [4]. The ability to create carbon nanostructures such as carbon nanofibers (CNF) and patterns with controlled dimensions, position and ordering, is crucial for engineering all-carbon devices [5,6]. Currently, CNFs and other nanostructured carbon can be manufactured via either catalyzed vapor-growth [7] or pyrolysis of nanostructured polymer precursors mainly based on polyacrylonitrile (PAN), including electrospun PAN fibers [8] and self-assembled PAN-containing block copolymers [9,10]. For these methods, the as-made carbon structures lack controlled ordering, particularly within the substrate plane. In contrast, precisely ordered carbon micro- and nanostructures were demonstrated by pyrolyzing patterned polymer precursors that had been fabricated with soft lithography [11], e-beam lithography [12], as well as nanoimprint lithography (NIL) [13]. For practical applications, soft lithography and e-beam lithography suffer from low patterning resolution or low processing throughput, respectively. NIL, on the other hand, possesses both the high resolution and throughput for creating well-controlled precursor patterns [14]. However, current NIL-based fabrication routes rely on UV-induced crosslinking of the resist, which requires that either the substrate or the template be transparent to UV [13]. Here, we report the use of thermal-embossing NIL (TE-NIL) to directly fabricate PAN films that can be subsequently cyclized and carbonized to yield highly uniform carbon patterns and nanoribbons over a large area. Most interestingly, we show that the orientation of the crystallites in the carbon nanostructures is uniquely controlled by the deformation mechanism of the PAN precursor during the imprinting process.

PAN is one of the major organic precursors used for manufacturing carbon fibers (with diameters around several microns) due to its high carbon yield and solution processability for fiber-drawing. Strangely, PAN has not yet been considered as an NIL resist to create patterned films as the precursor for nanostructured carbons. The lack of efforts in this endeavor might be related to the fact that PAN homopolymer is rarely melt-processed, since PAN chains degrade before they reach the melt state with increase of temperature [15]. The degradation process, commonly referred to as “cyclization”, turns linear PAN chains into thermally stable “ladder-like” rigid conjugated structures that do not flow [16]. Therefore, PAN indeed appears to be unsuited for TE-NIL as it relies on the squeeze flow of the resist material during imprinting [17]. We show that not only is PAN an ideal resist for TE-NIL but also that the cyclization process helps stabilize the imprinted PAN structures

* Corresponding authors.
E-mail addresses: zheng.zhang@colorado.edu (Z. Zhang), yifu.ding@colorado.edu (Y. Ding).

0032-3861/$ – see front matter © 2013 Elsevier Ltd. All rights reserved.
http://dx.doi.org/10.1016/j.polymer.2013.07.076

during the heat treatment, yielding excellent carbon nanostructures, which cannot be achieved by other non-crosslinkable thermoplastic polymers.

2. Experimental

Atactic PAN with an average molecular weight of 150,000 g mol^{-1} was purchased from Sigma–Aldrich Co. LLC., and used as received. The glass transition temperature (121 °C, T_g) and cyclization reaction temperature (307.1 °C, T_{cyc}) of the as-received material were determined from the first scan of Differential Scanning Calorimetry (DSC) with a NETZSCH DSC 204F1 in a nitrogen-filled chamber at a scanning rate of 10 °C min^{-1} (Supporting Information, Fig. S1(a)).

PAN films were first spin-coated from a 5 wt% solution in dimethylformamide (DMF) onto 380-microns-thick silicon substrates, which had been priorly treated with oxygen plasma. The as-cast films were then annealed at 50 °C (below the T_g of PAN) in a vacuum oven for 1 h in order to remove the remaining solvent.

Line-and-space grating patterns were replicated from a silicon mold onto the PAN film surfaces under a pressure of 6 MPa at 190 °C for 500 s, via Thermal Embossing Nanoimprint Lithography (TE-NIL) on an Eitre 3 (Obducat Inc.) nanoimprinter. The silicon mold patterns had a pattern height of 240 nm, a periodicity of 834 nm and a line-to-space ratio of 1. A low surface energy self-assembled layer (tridecafluoro-1,1,2,2-tetrahydrooctyl trichlorosilane, purchased from Sigma–Aldrich Co. LLC.) was deposited on the silicon mold via vapor deposition, prior to NIL, which effectively facilitated the release of the mold from the imprinted PAN at room temperature.

Reactive Ion Etching (RIE) was carried out on the as-imprinted PAN samples with a Plasma-Therm 540/540 Dual Chamber RIE vacuum system, at a pressure of 20 Pa and power of 150 W, in order to remove the residual layers. The only etchant used was oxygen at a constant flow-rate of 8.3×10^{-8} m^3 s^{-1} (5 sccm).

The as-fabricated PAN patterns/nanoribbons were thermally stabilized (cyclized) at 220 °C in air for 2 h on an STC200 hot-stage (Instec, Inc.) with a temperature stability of 0.1 °C. Carbonization was carried out by pyrolysis of the stabilized PAN patterns/nanoribbons in an argon-filled Lindberg Blue M® Tube Furnace (Thermo Fisher Scientific Inc.), by programmed heating with a temperature ramp of 5 °C/min from ambient temperature to a final temperature of 1000 °C, a 1 h hold and a ramp back to ambient temperature at 5 °C/min.

The PAN films/nanoribbons were characterized with a Dimension 3100 atomic force microscope (AFM, Bruker Corp.) and a JEOL JSM-7401F field emission scanning electron microscope (FE-SEM). An FIB (FEI, NOVA200 dual beam system) was used for high resolution transmission electron microscope (HR-TEM) sample cross-sectioning. An FEI Tecnai F20 operated at 200 keV was used for TEM imaging. Digital Micrograph software was used for the analysis of selected area electron diffraction (SAED) and fast Fourier transform (FFT). Raman spectra were obtained with a Jobin Yvon Raman spectrometer, model Olympus BX41 (Horiba, Edison, NJ), with an excitation wavelength of 532.16 nm.

3. Results and discussion

The cyclization reaction temperature (T_{cyc}) of the atactic PAN used in this study was determined to be 307.1 °C (Supporting Information, Fig. S1(b)), which was higher than the measured glass transition temperature (T_g) of 121 °C (Supporting Information, Fig. S1(a)) but lower than the predicted melting point (T_m) of ~320 °C [15]. As described below, PAN can be readily imprinted with TE-NIL at a temperature between T_g and T_{cyc}. Fig. 1(a) illustrates the fabrication routes for creating a carbon grating pattern (Route 1), as well as an array of isolated, well-aligned carbon nanoribbons (Route 2). Both routes started with spun-cast PAN thin-films with an average thickness of ~350 nm and a root mean square (RMS) roughness of ~47 nm (Supporting Information, Fig. S2). The roughness arose from the high viscosity of the PAN/DMF solution used for spin-coating and/or the partial crystallization of the PAN. TE-NIL was carried out by pressurizing (6 MPa) a silicon mold against the PAN thin-film at 190 °C for 500 s,

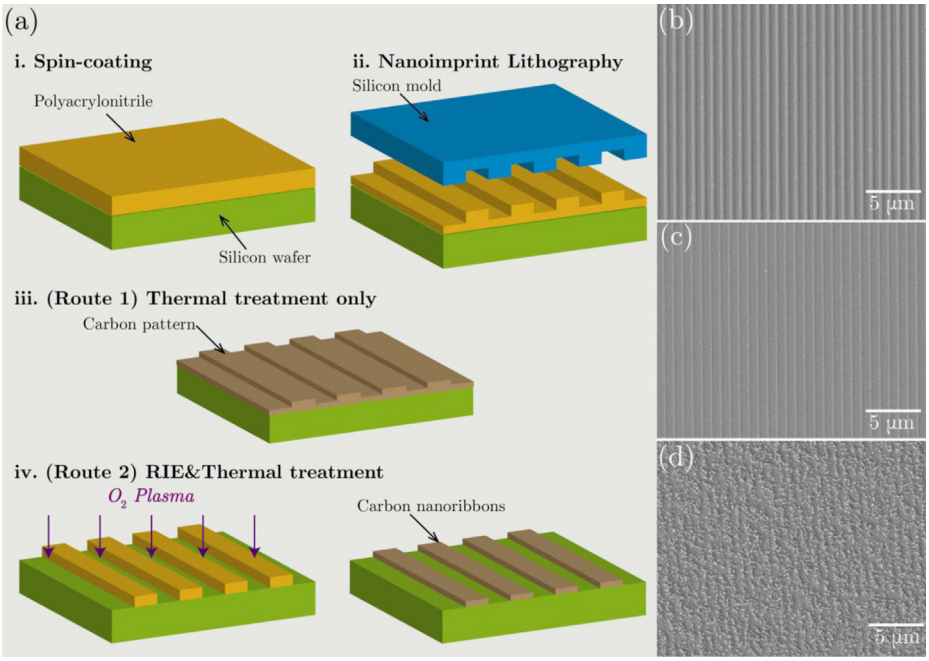

Fig. 1. (a) A schematic of the procedures for fabricating carbon patterns (Route 1: i → ii → iii) and carbon nanoribbons (Route 2: i → ii → iv) from PAN precursor; SEM images of the PAN-derived (b) carbon pattern and (c) carbon nanoribbons; and (d) carbon structure derived from carbonizing poly(methyl methacrylate) patterned lines, following Route 2.

replicating the line-and-space grating pattern from the silicon mold onto the PAN film, as schematically shown in Fig. 1(a)ii. The imprinted PAN pattern had a height of ~240 nm, a line-to-space ratio of 1 and a periodicity of 834 nm (Fig. 2(a)), confirming a faithful replication of the mold pattern (See Fig. 2(a) and Fig. S3 of Supporting Information).

At the imprinting temperature of 190 °C, solution-cast bulk PAN films show a storage modulus of ~46 MPa [18]. Because of the fast evaporation of the solvent during spin-coating, it was most likely that the crystallinity of spun-cast PAN thin films would be lower than that of bulk PAN films (~30%) [19]. Consequently, the effective rubbery modulus of PAN films under NIL conditions was expected to be lower than that of the bulk, allowing for sufficient viscoelastic deformation of PAN to fill in the mold cavities under a 6 MPa pressure. Apparently, the PAN molecular chains were mobile enough for high-fidelity pattern replication at a temperature lower than T_{cyc}.

The AFM height image and the corresponding cross-sectional profile of the as-imprinted PAN pattern, as well as those of the subsequent processing steps, are shown in Fig. 2. The as-imprinted PAN had a residual layer thickness of ~230 nm, as determined by the AFM measurements on a scratched PAN pattern (Supporting Information, Fig. S3). In Route 2, the residual layer was removed with RIE, as confirmed by AFM measurements (Supporting Information, Fig. S4), which resulted in an array of isolated PAN nanoribbons (Fig. 1(a)iv). Both the as-imprinted PAN and etched PAN were then cyclized and carbonized. Highly ordered carbon patterns and arrays of carbon nanoribbons were obtained, as shown in Fig. 1(b) and (c), respectively. Each step in the process was reproducible and the resultant structures were uniform over a large area (determined by the size of the mold). A photograph of the silicon mold together with cyclized PAN nanoribbons on a piece of silicon wafer and SEM images of larger views are shown in Figs. S5 and S6 of Supporting Information, respectively.

The unique self-catalytic cyclization reaction of PAN was crucial in successfully retaining the pattern features during the high temperature carbonization. For any other linear polymer, as-imprinted nanostructures would be flattened by surface-tension-induced Laplace pressure, once heated at a temperature above its T_g [20]. This would result in a flat carbon film or even ruptured structures caused by dewetting from the substrates [21] or capillary instability [20]. To examine this, we fabricated isolated poly(methyl methacrylate) (PMMA) fiber arrays using identical procedures as specified in Route 2. As expected, small carbon particles were obtained (Fig. 1(d)). The originally continuous PMMA grating lines could not survive the high temperature, although the morphology of these particulate carbon structures still roughly shows a grating-like ordering. Note that SiO_x is a wettable surface for PMMA. If a

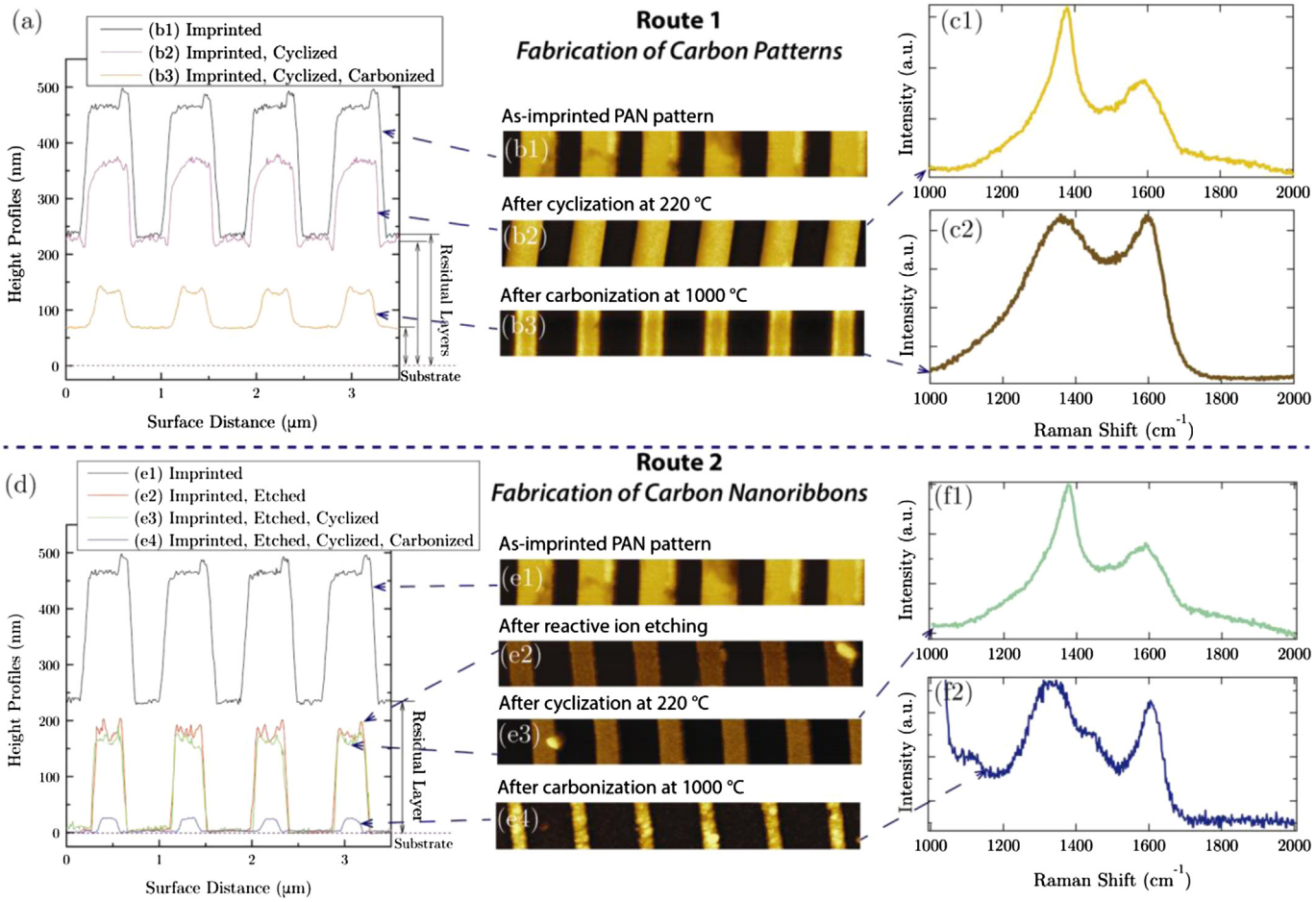

Fig. 2. (a) AFM height profiles corresponding to the height images of PAN (b1) imprinted; (b2) imprinted and cyclized; (b3) imprinted, cyclized and carbonized. (c1) and (c2) are the Raman spectra for the cyclized and carbonized samples, respectively, as indicated by the dashed arrows. (d) AFM height profiles corresponding to the height images of PAN (e1) imprinted; (e2) imprinted and etched; (e3) imprinted, etched and cyclized; (e4) imprinted, etched, cyclized and carbonized. (f1) and (f2) are the Raman spectra for the cyclized and carbonized samples, respectively. (b1)–(b3) collectively represent the sequential morphological changes for Route 1 shown in Fig. 1(a), whereas (e1)–(e4) represent those for Route 2. The dashed straight lines in (a) and (d) illustrate the substrate surface. The thicknesses of the residual layers are indicated by the double arrow.

non-wettable surface were used, the PMMA lines would be more prone to rupturing during heating.

Fig. 2 shows the cross-sectional profiles of the patterns at each processing step for creating both carbon patterns (a) and carbon nanoribbons (d). For Route 1, the pattern height shrank from 240 nm to ~150 nm after the cyclization process (Fig. 2(a)), with a slight reduction in the width and no change in the residual layer thickness. In contrast, the etched PAN nanoribbons (Route 2) did not show any clear dimensional changes during cyclization (Fig. 2(d)), which is consistent with previous observations of PAN fibers and films that only show slight volume shrinkage during cyclization [22]. The discrepancy in the shape change between the patterned PAN and the etched PAN is caused by the distribution of chain alignments within the imprinted PAN, as discussed below.

The deformation profile of PAN during the NIL process is schematically represented by the arrows in Fig. 3(a). The squeeze-flow-driven deformation caused the PAN chains to orient *vertically* within the mold cavity and *laterally* beneath the direct contact of the Si mold [17]. The alignment of PAN chains, regardless of the exact directions, gave rise to residual stresses within the structure because of the reduced conformational freedom of the chains [23,24]. Given enough time, PAN chains would have relaxed back to conformations of lower energies. However, both the presence of the PAN crystallites and pressurization prevented complete relaxation of the stretched chains, which were frozen within the patterns during the cooling.

However, when the temperature reached above the T_g of PAN during the cyclization process, the residual stresses were quickly relieved without the external pressure, reducing the pattern height from 240 to 160 nm; this behavior, also known as "elastic recovery", has been previously observed for nanoimprinted polymers [23,24]. Since the PAN chains were aligned mostly along the vertical direction within the as-imprinted pattern lines (i.e. mold cavities), the elastic recovery mostly occurred for chains along the vertical direction and little lateral shrinkage was observed (Fig. 2(a)). In contrast, the lateral alignment of the PAN chains were difficult to relax due to the restrictions from the substrate. For Route 2, the chain-aligned zones induced by the NIL process were vertically

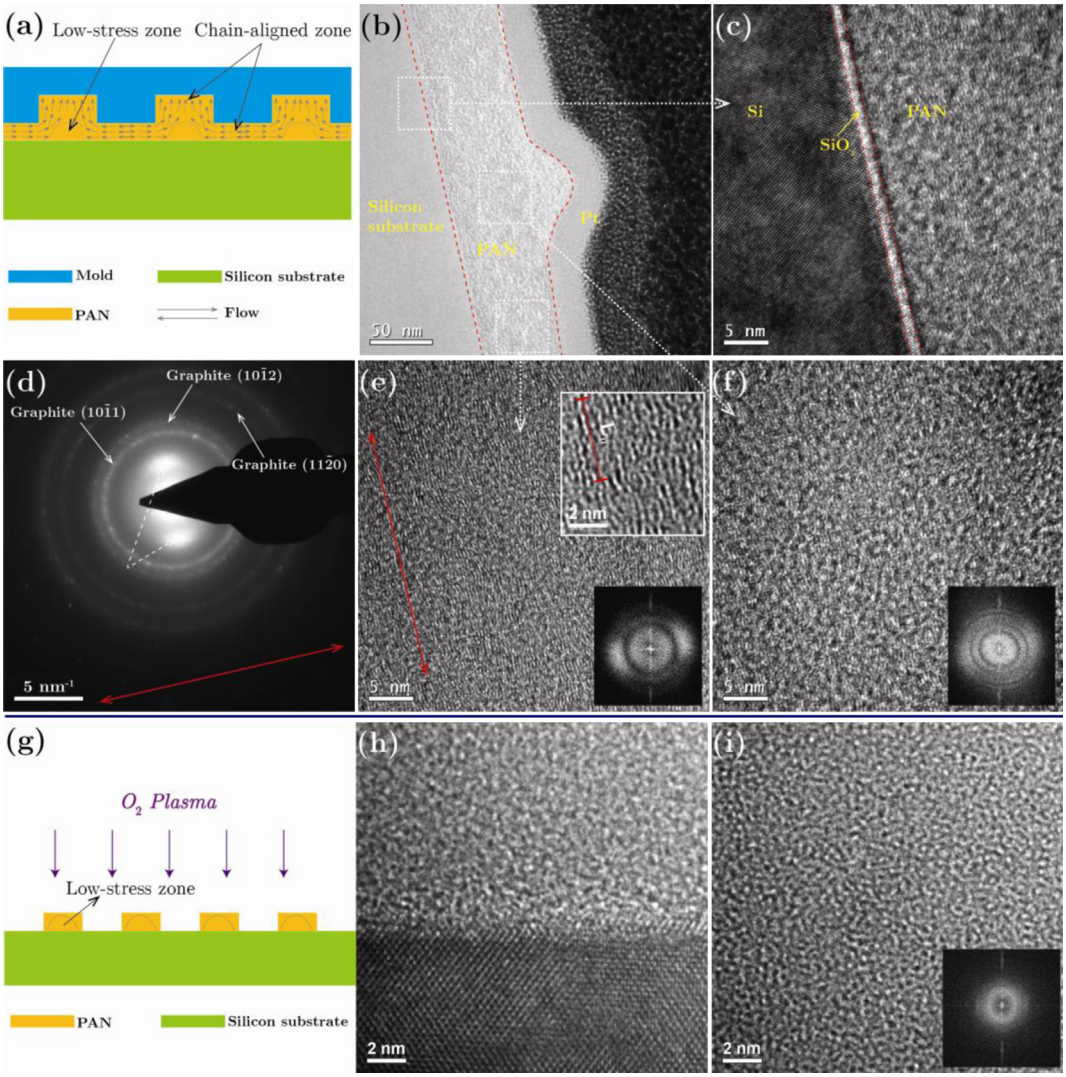

Fig. 3. (a) A schematic of the sample cross-section illustrating the squeeze-flow during imprinting; (b) TEM image of the cross-section of a carbon pattern; (c, e, f) high resolution views of the areas indicated with dashed-squares in (b); (d) an electron diffraction pattern of the cross-section. The insets of (e) and (f) are their corresponding FFTs. The red arrows in (d) and (e) indicate the direction in parallel with the substrate surface. (g) A schematic illustrating the cross-section of PAN after reactive ion etching; and TEM images of the cross-section of a carbon nanoribbon at (h) the ribbon/substrate interface and (i) the nanoribbon itself. The inset of (i) is its FFT. (For interpretation of the references to color in this figure legend, the reader is referred to the web version of this article.)

etched away during the directional RIE (Fig. 3(a) and (g)), resulting in isolated PAN nanoribbons with a height of ~190 nm and a width of ~370 nm (Fig. 2(d) and (e2)). In the absence of residual stresses, no significant dimensional changes due to elastic recovery were observed for the PAN nanoribbons during cyclization (Fig. 2(d)).

In the last step, the cyclized PAN patterns and nanoribbons were carbonized, removing the non-carbon heteroatoms. This mass loss caused a dramatic reduction in the pattern dimensions for both samples, as shown in Fig. 2. Overall the volume shrinkage was estimated to be ~70% for the PAN pattern and ~84% for the PAN nanoribbons. Carbon nanoribbons with a width of ~253 nm and height of ~26 nm were successfully obtained. The Raman spectra for the cyclized PAN pattern/nanoribbons and the carbon pattern/nanoribbons are presented in Fig. 2(c1)/(f1) and (c2)/(f2), showing the characteristic "D-band" at ~1360 cm^{-1} and "G-band" at ~1590 cm^{-1}. The D-band is associated with disordering on the surface or within the structures [25]. In contrast, the G-band is assigned to the sp^2 stretch vibration in the cyclized conjugated structures [26], whereas it is assigned to the doubly degenerated E_{2g} mode of graphite in the carbonized structures [27]. Overall, the Raman spectra of the carbonized patterns were similar to those of the PAN film carbonized at 1020 °C [28] and the SU-8 films carbonized at 1000 °C [12].

The intensity ratio, I_G/I_D, of the carbonized PAN is higher than that of the cyclized one, indicating that more ordered graphitic structures were formed. For the carbon patterns, the in-plane crystallite size, L_a, is estimated to be ~5 nm, using L_a (nm) = $C(\lambda_{Laser})\cdot(I_G/I_D)$, where $C(\lambda_{Laser})$ equals 5.0 nm for the excitation wavelength (532.16 nm) used in this study [29,30]. This is consistent with the TEM measurements (Fig. 3(e)). In comparison, I_G/I_D of the carbon nanoribbons (Fig. 2(f2)) is much lower than the carbon patterns, suggesting that the degree of disordering in the carbon nanoribbons is higher, which is also consistent with the TEM images (Fig. 3(i)). Note that the additional band found in Fig. 2(f2) below 1200 cm^{-1} was resultant from the silicon substrate. The strong intensity of this additional band and the high signal-to-noise ratio were due to the minuscule volume of carbon in the carbon nanoribbon samples.

In principle, alignment of the PAN chains would lead to a similar orientation of carbon crystallites after pyrolysis. Zhou et al. found that, for electrospun PAN fibers, the orientation was not preserved in the low pyrolysis temperature (1000 °C) and only a high pyrolysis temperature (2200 °C) led to oriented graphitization of the fibers [31]. In the following, we show that different orientations of carbon crystallites were indeed observed between the carbon patterns and the nanoribbons pyrolyzed at even 1000 °C. Fig. 3 shows the TEM images of the cross-sections of the carbon pattern and nanoribbons. For TEM sample preparation, Platinum (Pt) was deposited onto the surface of the carbon pattern as a protective layer against Ga ions, before Focused Ion Beam (FIB) cross-sectioning. In between the silicon substrate and the Pt layer is the PAN-derived carbon, labeled as "PAN" in the figure; the hump in the carbon pattern is an actual single carbon pattern line.

Fig. 3(c), (e) and (f) show HR-TEM images at the substrate/residual layer interface, residual layer under the mold contact, and right underneath the pattern lines, correspondingly. Overall, the in-plane domain size (L_a, as labeled in the inset of Fig. 3(e)) of the carbon crystallites (~5 nm) was consistent with both the estimation from the Raman spectra discussed above and with previous reports of PAN-derived carbon [28]. Excellent contact was observed between the carbon patterns and the substrate, whereas carbon microstructures precursored with crosslinked organic networks suffer from adhesion issues [11]. Partial in-plane alignment of the carbon crystallites was also observed, consistent with the deformation profile of PAN during TE-NIL (Fig. 3(a)). The in-plane alignment was most evident at regions directly underneath the mold contact (Fig. 3(e)), where the deformation gradient was the largest [17]. In contrast, no evident orientation among the crystallites at regions immediately beneath the pattern lines was observed (Fig. 3(f)), due to the elastic recovery of the aligned chains and the intrinsically low deformation gradient in this region.

Fig. 3(d) shows the SAED pattern of the carbonized PAN patterns, using an aperture over the chain-aligned area (Fig. 3(e)). The diffraction rings, as indexed in reference to hexagonal crystal graphite, indicate the polycrystalline nature of the carbon structures. In comparison, carbonized planar PAN films displayed an amorphous pattern [28]. The two diffused spots indicated by the dashed arrows, which were absent in the literature data [28], correspond to a *d*-spacing of 0.38 nm. This was likely resultant from the correlation between the turbostatic carbonaceous layers, according to Bourrat et al.'s calculation [32]. For completely random carbon layers stacked together with no preferred orientation, rings would be observed instead of spots [33]. The correlation length between the carbon layers was estimated to be ~0.38 nm from the fast Fourier transform (FFT) analysis of Fig. 3(e), which is consistent with the aforementioned SAED pattern. The turbostatic carbon layers were not completely graphitic but contained a nitrogen weight fraction less than 2.5% [34]. In comparison, the chain-aligned zones in the as-imprinted PAN were completely etched away during RIE, leaving more randomly oriented PAN chains with low residual stresses (Fig. 3(g)). Indeed, the cross-sectional TEM images for the nanoribbons at regions near the substrate (Fig. 3(h)) and within the lines show that the carbon is more amorphous than that in Fig. 3(e) and the crystallites are randomly oriented in both regions, consistent with the Raman spectra discussed above.

4. Conclusions

In summary, we show that PAN homopolymer, although incapable of flow in the melt state, could be directly imprinted with high fidelity and used as a precursor to fabricate lithographically defined carbon patterns and carbon nanoribbons. The unique cyclization process of PAN was crucial for maintaining the pattern features of the patterned PAN precursors, which cannot be achieved with other linear polymers. The deformation profile of the PAN during the TE-NIL process resulted in a distribution of aligned PAN chains within the patterns, which led to a similar anisotropic correlation of the carbon crystallites in the carbonized structures. Therefore, the direct use of PAN as a patterning resist and carbon precursor enables fabrication of well-defined carbon patterns and nanoribbons over a large area at low cost, which is beneficial to a broad range of carbon-based nanotechnologies.

Acknowledgments

The authors are grateful to Lauren Cantley, Brian Francisco and Dr. Ji Woo Kim for their help and useful discussions. We thank Prof. Scott Bunch for the use of the CVD furnace. We acknowledge the funding support from the National Science Foundation under grant number CMMI-1031785 and from the U.S. Department of Energy under subcontract number NFT-8-88527-01 through the DOE Office of Energy Efficiency and Renewable Energy Office of the Vehicle Technology Program. Z.Z. gratefully acknowledges the support from the donors of the Beverly Sears Graduate Student Grant at University of Colorado. Acknowledgment is made to the Fundamental R&D Program for Technology of World Premier Materials funded by the Ministry of Knowledge Economy, Republic of Korea (10037919).

Appendix A. Supplementary data

Supplementary data related to this article can be found at http://dx.doi.org/10.1016/j.polymer.2013.07.076.

References

[1] Park S, Kim Y-S, Kim WB, Jon S. Carbon nanosyringe array as a platform for intracellular delivery. Nano Letters 2009;9:1325–9.
[2] Whitby M, Cagnon L, Thanou M, Quirke N. Enhanced fluid flow through nanoscale carbon pipes. Nano Letters 2008;8:2632–7.
[3] Zheng G, Yang Y, Cha JJ, Hong SS, Cui Y. Hollow carbon nanofiber-encapsulated sulfur cathodes for high specific capacity rechargeable lithium batteries. Nano Letters 2011;11:4462–7.
[4] Avouris P, Chen Z, Perebeinos V. Carbon-based electronics. Nature Nanotechnology 2007;2:605–15.
[5] Nguyen-Vu TDB, Chen H, Cassell AM, Andrews R, Meyyappan M, Li J. Vertically aligned carbon nanofiber arrays: an advance toward electrical-neural interfaces. Small 2006;2:89–94.
[6] Rahman S, Yang H. Nanopillar arrays of glassy carbon by anodic aluminum oxide nanoporous templates. Nano Letters 2003;3:439–42.
[7] Takagi D, Kobayashi Y, Hibino H, Suzuki S, Homma Y. Mechanism of gold-catalyzed carbon material growth. Nano Letters 2008;8:832–5.
[8] Inagaki M, Yang Y, Kang F. Carbon nanofibers prepared via electrospinning. Advanced Materials 2012;24:2547–66.
[9] Kowalewski T, Tsarevsky NV, Matyjaszewski K. Nanostructured carbon arrays from block copolymers of polyacrylonitrile. Journal of the American Chemical Society 2002;124:10632–3.
[10] Tang C, Tracz A, Kruk M, Zhang R, Smilgies D-M, Matyjaszewski K, et al. Long-range ordered thin films of block copolymers prepared by zone-casting and their thermal conversion into ordered nanostructured carbon. Journal of the American Chemical Society 2005;127:6918–9.
[11] Schueller OJ, Brittain ST, Whitesides GM. Fabrication of glassy carbon microstructures by soft lithography. Sensors and Actuators A: Physical 1999;72:125–39.
[12] Du R, Ssenyange S, Aktary M, McDermott MT. Fabrication and characterization of graphitic carbon nanostructures with controllable size, shape, and position. Small 2009;5:1162–8.
[13] Penmatsa V, Kawarada H, Wang C. Fabrication of carbon nanostructures using photo-nanoimprint lithography and pyrolysis. Journal of Micromechanics and Microengineering 2012;22:045024.
[14] Guo LJ. Nanoimprint lithography: methods and material requirements. Advanced Materials 2007;19:495–513.
[15] Krigbaum WR, Tokita N. Melting point depression study of polyacrylonitrile. Journal of Polymer Science 1960;43:467–88.
[16] Bashir Z. A critical review of the stabilisation of polyacrylonitrile. Carbon 1991;29:1081–90.
[17] Rowland HD, Sun AC, Schunk PR, King WP. Impact of polymer film thickness and cavity size on polymer flow during embossing: toward process design rules for nanoimprint lithography. Journal of Micromechanics and Microengineering 2005;15:2414–25.
[18] Guo H, Rasheed A, Minus ML, Kumar S. Polyacrylonitrile/vapor grown carbon nanofiber composite films. Journal of Materials Science 2008;43:4363–9.
[19] Hobson RJ, Windle AH. Crystalline structure of atactic polyacrylonitrile. Macromolecules 1993;26:6903–7.
[20] Zhang Z, Ahn DU, Ding Y. Instabilities of PS/PMMA bilayer patterns with a corrugated surface and interface. Macromolecules 2012;45:1972–81.
[21] Reiter G. Unstable thin polymer films: rupture and dewetting processes. Langmuir 1993;9:1344–51.
[22] Hou Y, Sun T, Wang H, Wu D. A new method for the kinetic study of cyclization reaction during stabilization of polyacrylonitrile fibers. Journal of Materials Science 2008;43:4910–4.
[23] Ding Y, Ro HW, Douglas JF, Jones RL, Hine DR, Karim A, et al. Polymer viscoelasticity and residual stress effects on nanoimprint lithography. Advanced Materials 2007;19:1377–82.
[24] Ding Y, Ro HW, Alvine KJ, Okerberg BC, Zhou J, Douglas JF, et al. Nanoimprint lithography and the role of viscoelasticity in the generation of residual stress in model polystyrene patterns. Advanced Functional Materials 2008;18:1854–62.
[25] Wang Y, Alsmeyer DC, McCreery RL. Raman spectroscopy of carbon materials: structural basis of observed spectra. Chemistry of Materials 1990;2:557–63.
[26] Schwan J, Ulrich S. Raman spectroscopy on amorphous carbon films. Journal of Applied Physics 1996;80:440.
[27] Tuinstra F, Koenig JL. Raman spectrum of graphite. The Journal of Chemical Physics 1970;53:1126–30.
[28] Renschler CL, Sylwester AP, Salgado LV. Carbon films from polyacrylonitrile. Journal of Materials Research 1989;4:452–7.
[29] Cançado L, Jorio A, Pimenta M. Measuring the absolute Raman cross section of nanographites as a function of laser energy and crystallite size. Physical Review B 2007;76:064304.
[30] Knight DS, White WB. Characterization of diamond films by Raman spectroscopy. Journal of Materials Research 1989;4:385–93.
[31] Zhou Z, Lai C, Zhang L, Qian Y, Hou H, Reneker DH, et al. Development of carbon nanofibers from aligned electrospun polyacrylonitrile nanofiber bundles and characterization of their microstructural, electrical, and mechanical properties. Polymer 2009;50:2999–3006.
[32] Bourrat X, Trouvat B, Limousin G, Vignoles G, Doux F. Pyrocarbon anisotropy as measured by electron diffraction and polarized light. Journal of Materials Research 2000;15:92–101.
[33] Neidhardt J, Hultman L, Czigány Z. Correlated high resolution transmission electron microscopy and X-ray photoelectron spectroscopy studies of structured CNx ($0<x<0.25$) thin solid films. Carbon 2004;42:2729–34.
[34] Ra EJ, Raymundo-Piñero E, Lee YH, Béguin F. High power supercapacitors using polyacrylonitrile-based carbon nanofiber paper. Carbon 2009;47:2984–92.